Characterizing the occurrence and spatial heterogeneity of liquid, ice and mixed phase low-level clouds over the Southern Ocean using in situ observations acquired during SOCRATES

John J. D'Alessandro[1,2], Greg M. McFarquhar[1,2], Wei Wu[1], Jeff L. Stith[3], Jorgen B. Jensen[3], Robert M. Rauber[4]

[1]Cooperative Institute for Mesoscale Meteorological Studies, University of Oklahoma: Norman, OK, USA, 73072.

[2]School of Meteorology, University of Oklahoma, Norman, OK, USA 73072

[3]National Center for Atmospheric Research, Research Aviation Facility/Earth Observing Laboratory: Boulder, CO, USA, 80307

[4]Department of Atmospheric Sciences, University of Illinois at Urbana–Champaign, Urbana, Illinois, USA, 61081

Corresponding Author: Greg M. McFarquhar (mcfarq@ou.edu)

Key Points:

- A high occurrence frequency of supercooled liquid water is observed in low level clouds over the Southern Ocean between Tasmania and the Antarctic.
- Mixed phase samples are the most spatially heterogeneous phase compared with liquid and ice phase within low level clouds over this region.

Abstract

Supercooled liquid water (SLW) and mixed phase clouds containing SLW and ice over the Southern Ocean are poorly represented in global climate and numerical weather prediction models. Observed SLW exists at lower temperatures than threshold values used to characterize its detrainment from convection in model parameterizations, and processes controlling its formation and removal are poorly known. High resolution observations are needed to better characterize the SLW over the Southern Ocean. This study characterizes the frequency and spatial distribution of different cloud phases (liquid, ice and mixed) using in situ observations acquired during the Southern Ocean Clouds, Radiation, Aerosol Transport Experiment Study (SOCRATES). Cloud particle phase is identified using multiple cloud probes. Results show occurrence frequencies of liquid phase samples up to 70% between -20° and 0°C, and of ice phase samples up to 10% between -5° and 0°C. Cloud phase spatial heterogeneity is determined by relating the total number of 1 second samples from a given cloud to the number of segments whose neighboring samples are the same phase. Mixed phase conditions are the most spatially heterogeneous from -20° to 0°C, whereas liquid phase conditions from -10° to 0°C and ice phase conditions from -20° to -10°C are the least spatially heterogeneous. Greater spatial heterogeneity is associated with broader distributions of vertical velocity. Decreasing droplet concentrations and increasing number-weighted mean liquid diameters occur within mixed phase clouds as the liquid water fraction decreases, possibly suggesting preferential evaporation of smaller drops during the Wegener-Bergeron-Findeisen process.

1. Introduction

Clouds over the Southern Ocean (SO) strongly influence the energy budget over this region, with satellite observations showing an annual mean spatial fraction around 80%–90% (e.g., Kay et al., 2012; Matus & L'Ecuyer, 2017; McCoy et al., 2014) . Climate models struggle to correctly simulate radiative fluxes over the SO (50–80°S), commonly underestimating reflected shortwave radiation in part because they (e.g., Bodas-Salcedo et al., 2016; Cesana & Chepfer, 2013; Kay et al., 2016; Trenberth & Fasullo, 2010; Wang et al., 2018) produce lower cloud fraction and less supercooled liquid water (SLW, liquid water at temperatures below 0°C) than observed. Similar problems have been noted in output from higher-resolution models (e.g., Huang et al. 2014, 2015; Naud et al. 2014).

Supercooled liquid water (SLW) plays a critical role in determining cloud radiative forcing (e.g., Ceppi et al., 2014; Lawson & Gettelman, 2014; Shupe & Intrieri, 2004), cloud feedbacks (e.g., Gettelman & Sherwood, 2016; Tsushima et al., 2006), and equilibrium climate sensitivity (e.g., Frey & Kay, 2017; Tan et al., 2016). A negative cloud phase feedback resulting from the transition of ice to liquid under surface heating was first proposed by Mitchell et al. (1989). Additional considerations must be made for mixed phase clouds by characterizing the mass fractions and spatial distribution of ice and liquid phases, as well as their degree of mixing, which can substantially impact the radiation budget (e.g., Sun & Shine, 1994; McFarquhar & Cober, 2004). Commonly referred to as the Wegener–Bergeron–Findeisen (WBF) process, ice particles grow at the expense of neighboring SLW droplets given that the equilibrium water vapor pressure with respect to liquid is greater than that with respect to ice (Bergeron, 1928, 1935; Findeisen, 1938, 1940; Wegener, 1911). Several microphysical and dynamical mechanisms have been introduced to describe mixed phase clouds and their evolution (e.g., Korolev & Field, 2008; Jackson et al., 2012; Korolev et al., 2017; Kreidenweis et al., 2018). However, considerable work is required to constrain such mechanisms and further improve the understanding of these clouds. For example, although mixed phase clouds are thermodynamically unstable due to the differences in the saturation vapor pressures of liquid and ice, they are commonly observed to persist for hours or even days in the high latitudes (e.g., Morrison et al., 2011; Verlinde et al., 2007).

The spatial distribution of liquid and ice particles can have major impacts on the WBF process (Korolev & Isaac, 2006; Korolev et al., 2003). Further, the relatively coarse spatial resolutions of climate models require smaller scale/subgrid cloud heterogeneities to be parameterized. Differences in these parameterizations can significantly impact simulated cloud lifetimes and microphysical properties (e.g., Storelvmo et al., 2008; Zhang et al., 2019). Previous studies have examined the spatial heterogeneity of cloud phase at different locations (e.g., Chylek et al., 2006; Field et al., 2004; McFarquhar et al., 2007a; Stubenrauch et al., 1999) including the SO (D'Alessandro et al., 2019; Zaremba et al., 2020). However, most of these studies merely comment qualitatively on observed heterogeneity from time series and vertical cross sections. Improved characterizations of phase spatial heterogeneity are crucially needed to provide clear and definite results for the evaluation of model simulations. This study uses in situ observations from the 2018 Southern Ocean Clouds, Radiation, Aerosol Transport Experimental Study (SOCRATES) to characterize the frequency and spatial distributions of cloud phases over the SO. Section 2 introduces the in situ instrumentation and data processing techniques, Section 3 presents the findings, Section 4 provides further interpretation of the results, and Section 5 summarizes the key findings.

2. Dataset and experimental setup

2.1 In situ observations

This study uses 1-Hz airborne measurements collected from the National Science Foundation (NSF)/National Center for Atmospheric Research (NCAR) Gulfstream-V (GV) research aircraft during SOCRATES. SOCRATES was based out of Hobart, Tasmania and took place from 15 January to 28 February 2018, sampling over the SO from 42° to 62°S and from 133° to 163°W. Fifteen research flights were conducted during SOCRATES. The aircraft primarily targeted cold sector boundary layer clouds. Flight plans were designed to ideally sample 10-minute level legs above cloud, in cloud, and below cloud, followed by sawtooth legs to obtain vertical profiles. Additional details on flight objectives and analyses can be found in McFarquhar et al. (2021). Observations are restricted to temperatures less than 0°C to exclude warm clouds (i.e., clouds with no ice or SLW), so that approximately 14 hours (7,680 km) of in-cloud data between -40° and 0°C were available for analysis. The flights during SOCRATES primarily sampled the cold sector of cyclones with some passes through frontal systems, mostly associated with strong westerly flow over the SO (McFarquhar et al., 2021). These synoptic-scale conditions coupled with a cool ocean surface led to frequent cloud cover over the SOCRATES flight domain, including many cases of low-level and midlevel stratus and stratocumulus. Multilayer stratus and single-layer stratocumulus were frequently observed in several flights. Temperature was measured using a fast-response Rosemount temperature probe; for steady conditions the estimated accuracy and precision are 0.3K and 0.01K, respectively. Table 1 includes information of all the instrumentation used in this study, all of which are introduced and discussed further below.

A suite of cloud probes was installed on the G-V. Probes for measuring size distributions included a 2-Dimensional Stereo probe (2DS, manufactured by SPEC, Inc.), a 2-Dimensional Cloud probe (2DC, a Particle Measuring Systems instrument, modified for fast response), a Precipitation Imaging Probe (PIP, manufactured by Droplet Measuring Techniques, DMT), a Particle Habit Imaging and Polar Scattering probe (PHIPS HALO) and a DMT Cloud Droplet Probe (CDP). Second-by-second comparison of the size distributions of the 2DC and 2DS showed marked differences between probes. Examination of particle images showed degraded 2DC image quality occurred for more than half of the flight hours due to fogging, and hence these data were unusable. A problem with the time record on the PIP prevented use of the PIP image data, and hence information about the size distributions of large particles was not available. Thus, the base size distributions were characterized by a combination of the CDP and 2DS data. Data from the CDP were used to characterize particles with maximum dimension (hereafter size D) ranging from 2 to 50 µm. Although the 2DS can nominally detect particles with D ranging from 10 to 1280 µm, only particles having maximum dimensions (D_{2DS}) greater than or equal to 50 µm were used because of a small and highly uncertain depth of field for D_{2DS} < 50 µm (e.g., Baumgardner & Korolev, 1997). The SOCRATES 2DS size distributions and particle morphological data (Wu & McFarquhar, 2019) were determined using the University of Illinois/Oklahoma Optical Probe Processing Software (UIOOPS, McFarquhar et al., 2017, 2018), and include corrections for removal of shattered artifacts (Field et al., 2003; Field et al., 2006). Mass distribution functions are determined using the habit-dependent mass-size relationships summarized by Jackson et al. (2012, 2014) for the different particle habits that are identified in UIOOPS (McFarquhar et al., 2018) following a modified Holroyd (1987) approach.

A 1-s sample is identified as in-cloud if either of the following two conditions is met: 1) CDP measurements reporting mass concentration (M_{CDP}) greater than 10^{-3} g m^{-3} where M_{CDP} is estimated from the size distributions assuming all particles are spherical water droplets, or 2) 2DS measurements report number concentrations of at least one particle having $D_{2DS} > 50$ µm (N_{2DS}). The rest of the time periods are defined as outside of cloud. Although this definition of cloud allows for thinner and more tenuous cloud than previous studies that assumed mass thresholds of 0.01 g m^{-3} for identifying cloud (e.g., McFarquhar et al., 2007a), it allows thin layers at lower temperatures to be included in the analysis. Further, although M_{CDP} is not a well-defined quantity for ice clouds as forward scattering probes assume Mie theory and spherical particles in their sizing and the CDP does not properly sample non-spherical particles (McFarquhar et al., 2007b), a threshold based on M_{CDP} was chosen to eliminate sea spray (and other large aerosols) as confirmed by comparing time series with images from the forward-facing camera, which reported encounters with sea spray. The CDP threshold was also chosen by evaluating a joint frequency distribution controlled by mass and number concentrations (Figure A in supplementary material) and finding a significant bimodality, by which the modes are separated by M_{CDP} greater than and less than the threshold chosen, consistent with inspection of time series and the forward-facing camera of in-cloud samples and sea spray.

Liquid water was sampled by two instruments, a Rosemount icing detector (RICE), and a King-style hot wire instrument (KING; King et al. 1978, manufactured by Droplet Measurement Technologies (DMT)). The presence of small amounts of SLW can be ascertained from the Rosemount icing detector (RICE). The RICE is a metal protrusion which vibrates at a constant frequency; if supercooled droplets collide with it, the droplets freeze and alter the frequency of the vibrating rod. The output is translated into a voltage signal, which increases as more, or decreases as less (e.g., by sublimation) ice accumulates on the protrusion. The theoretical performance of the RICE is described in Mazin et al. (2001). The response of the instrument is dependent on airspeed, air density, and humidity as well as the sizes of droplets, as large drops may splash upon hitting the probe. Mazin et al. (2001; Figure 4a) suggest a theoretical threshold liquid water content limit of ~0.025 g m^{-3} or less at conditions similar to those sampled in this study; however, the response to liquid water may vary from probe-to-probe, requiring independent calibration for quantitative results. During the lower-level cloud conditions in SOCRATES, droplets were found to not freeze on the RICE protrusion for temperatures greater than -5˚C due to dynamic heating of the sensor. Further, data are not usable during the reheating cycle of the RICE that removes the frozen particles accumulated on the wire (e.g., Mazin et al., 2001), which are shown in Figure 1C where $dV/dt<0$ V s^{-1}. Thus, the RICE offers an independent detection of SLW conditions, but is not used here as a stand-alone quantitative measure of supercooled water concentrations. Sensitivity tests were performed to determine the best method to discern the cloud phase using the RICE probe in combination with data obtained from other probes, as discussed in the next section.

For results examining the characterization of mixed phase microphysical properties (Section 3.2), the KING probe was utilized. King et al. (1978) report a sensitivity of 0.02 g m$^{−3}$, a response time of better than 0.05 s and an accuracy of 5% at 1 g m$^{−3}$, but these parameters can vary depending on flight speed as discussed in McFarquhar et al. (2017) and Baumgardner et al. (2017). Similar to the RICE probe, the KING probe responds to smaller liquid droplets (e.g., volume-weighted mean diameter less than 0.15 mm as reported by Biter et al. (1987)) so it underestimates SLW in the presence of supercooled drizzle (e.g., Schwarzenboeck et al., 2009), but also can overestimate SLW in the presence of ice (Cober et al., 2001). Thus, the KING probe is best for measuring the liquid water contents in the presence of exclusively smaller drops, while estimates of SLW content in the presence of drizzle are best obtained by integrating the size distributions. Water vapor is measured using the 25-Hz Vertical Cavity Surface Emitting Laser (VCSEL) hygrometer (Zondlo et al., 2010), which has an accuracy and precision of ~6% and ≤1%, respectively. The calculation of relative humidity with respect to ice (*RHi*) is based on Murphy & Koop (2005). For temperatures from -40° to 0°C, the uncertainties in *RHi* range from 6% to 8%. Vertical velocity (*w*) is measured using the Radome Gust Probe in combination with pitot tubes and the differential Global Positioning System, where Cooper et al. (2016) report a net uncertainty in the standard measurement of vertical wind of 0.12 m s^{-1}, although this represents ideal sampling conditions. More information on the performance of the GV gust probe processing and other instrumentation performance is provided in the manager's report (EOL, 2018). The report describes methods that were used to correct for drift with altitude in the system, which likely increases the uncertainty, especially over the whole range of altitudes in SOCRATES (although the performance at constant altitudes should be steady). Further research on the performance of the system is planned to better document these uncertainties. The project manager's report also provides additional information on the processing and data quality issues related to the other routine instruments.

2.2 Determining cloud phase

Figure 1A shows normalized probability density functions of the RICE change in voltage (*dV/dt*) for different ranges of number concentrations from the CDP (N_{CDP}). Greater voltage changes are associated with greater liquid mass. Results show changes in voltage are positively skewed and noticeably greater for $N_{CDP} \geq 1$ cm^{-3}, suggesting that high N_{CDP} are generally liquid samples. This is consistent with previous studies (e.g., Lance et al., 2010; Heymsfield et al., 2011; Finlon et al., 2019) which have noted that a threshold in CDP concentrations can serve as a first estimate for the presence of SLW in the absence of information from other probes. Figure 1B shows a sharp bimodal distribution of N_{CDP} for temperatures less than -20˚C where more ice would be expected. Thus, a threshold value of $N_{CDP}\geq 1$ cm^{-3} is used to identify time periods where cloud particles with D < 50 μm are liquid. Examination of the CDP and RICE data confirmed that time periods with $N_{CDP}<1$ cm^{-3} correspond to minimal voltage responses from RICE, further suggesting low N_{CDP} corresponds with ice phase observations. Figure 1C shows vertical profiles of the RICE *dV/dt* for all in-cloud samples acquired during SOCRATES with results colored by N_{CDP}. The dashed line at 0.01 V s^{-1} roughly intersects between datapoints where N_{CDP}=0 (grey points), and N_{CDP}>0 (colored points) over most of the vertical column. The dotted line at 0.002 V s^{-1}, based on a previously proposed threshold to infer the existence of liquid (Heymsfield & Miloshevich, 1989), shows that this threshold would overestimate the frequency of liquid based on the CDP measurements, especially those at low temperatures. Thus, results presented here suggest a 0.01 V s^{-1} threshold is less susceptible to overestimating the frequency of liquid (for example, the large number of samples >0.002 V s^{-1} at temperatures less than -20°C where N_{CDP}=0 cm^{-3}).

The phase of the 2DS particles with D_{2DS}>50 um is calculated using multinomial logistic regression (MLR), which models nominal outcome variables. Logistic regression is commonly accepted as a successful method for classification (e.g., Bishop, 2006). Specifically, MLR produces the logarithmic odds of outcomes modeled as a linear combination of the predictor variables. Previously, this method was used to derive the habits of ice crystals from two-dimensional particle images using multiple optical array probes, including the 2DS (Praz et al., 2018). The 2DS provides two-dimensional particle imagery, of which 1362 s worth of particles with D_{2DS} > 50 μm were visually inspected and classified as either liquid, mixed or ice phase (i.e., the training set). Spherical particle images are assumed to be liquid drops whereas all other particles are assumed to be ice particles. The predictor variables used in MLR were M_{2DS}, N_{2DS}, number-weighted mean D_{2DS} ($Mean\ D_{2DS}$), standard deviation of D_{2DS} (σ_{D_2DS}), standard deviation of number concentrations in 10 μm bins (σ_{N_2DS}), the maximum particle D_{2DS} ($Max\ D_{2DS}$) and N_{CDP}. Since the presence of smaller cloud droplets (D<50 μm) was found to be a successful proxy for larger supercooled droplets (Heymsfield et al., 2011; Finlon et al., 2019; D'Alessandro et al., 2019), N_{CDP} was included as a predictor in the MLR. The phase having the highest likelihood of the three as determined by the MLR is selected. Additional visual inspection of a separate 1287 s worth of 2DS imagery was performed following the MLR analysis in order to evaluate its success (i.e., the validation set). A decision tree similar to that used for the 2DC in D'Alessandro et al. (2019) was developed for the 2DS and compared with results from the MLR as a baseline model. The Heidke skill score gives an indication of a prediction's success, where values approaching one indicate improving predictions and a value of 0 indicates the prediction performs as well as a randomized dataset. It was calculated as a multi-category forecast (one phase per category), of which further information of can be found in Jolliffe & Stephenson (2011). The MLR classification was found to perform well, as highlighted by Heidke skill scores of 0.88 and 0.68 for the MLR and baseline datasets, respectively. The phase flag was manually corrected for the "missed" predictions, including an additional 751 samples from further visual inspection of 2DS images showing spherical particles where neither the RICE nor CDP was flagged as liquid. The use of RICE and CDP as proxy data for the phase of particles having D>50 μm is believed to improve upon the MLR phase classification, as distributions of RHi for these cases center around 100%, most notably at temperatures less than -

20°C (Figure B in supplementary material). A flow chart highlighting phase categorization using the RICE, CDP and 2DS is shown in Figure 2. The phase is determined separately for cloud particles having D<50 μm (CDP and RICE) and D>50 μm (2DS). Thus, a sample is liquid when liquid is only reported for all particle sizes, and similarly for ice. A sample is mixed phase when both liquid and ice are reported. Cloud phase is determined every second, amounting to horizontal spatial resolutions of ~150 m depending on the aircraft flight speed.

A time series including 2DS images and cloud phase classification results is shown in Figure 3. Examples of images for all three phases are shown underlying the time series, where the images correspond with the overlying boxes. The top two rows show temperature, particle size distribution statistics from the 2DS ($Max\ D_{2DS}$ and $Mean\ D_{2DS}$) and N_{CDP}. The third row shows particle mass distribution functions from the 2DS over all available bin sizes and the fourth row shows cloud phase results. For the liquid case, $Max\ D_{2DS}$ reveals that SLW drops can often have D > 0.3 mm, consistent with observations that drizzle is sometimes present in low-level cloud regimes. $Mean\ D_{2DS}$ is exceptionally low (typically less than 0.2 mm), due to the vast majority of droplets having relatively small D_{2DS}. This is similarly observed for the mixed phase case, although in contrast $Max\ D_{2DS}$ far exceeds the sizes of supercooled drizzle drops due to the large ice particles observed that may preferentially grow due to riming or the larger supersaturation over ice compared to water. The ice phase case similarly has large $Max\ D_{2DS}$, and in contrast to the liquid and mixed phase case has much larger $Mean\ D_{2DS}$, since there is no longer a large concentration of smaller liquid drizzle particles. These variations in 2DS particle statistics highlight how the listed statistical parameters can be used to derive the phase of larger particles (D>50μm). Similarly, large segments of the mass distribution functions are relatively homogeneous, highlighting relatively static microphysical properties over short durations of observations having similar phase.

3. Results

3.1 Cloud phase frequency distributions

The relative frequency distribution of cloud phase as a function of temperature is shown in Figure 4. Cloud samples are primarily liquid phase at the highest temperatures, and ice phase at the lowest temperatures. Mixed phase samples are the most infrequent, which may be expected since the mixed phase is thermodynamically unstable. In fact, previous analyses have shown that mixed phase clouds, where the fraction of liquid water content to total water content is between 0.1 and 0.9, are not common (e.g., Korolev et al., 2003). This may also be related to the inability to discern the coexistence of ice and liquid particles having diameters less than 50 (due to CDP and RICE limitations) to 100 μm (due to coarse resolution of relatively small particles in 2DS particle imagery), which might result in an underestimation of mixed phase samples. Interestingly, ice-only observations were observed at temperatures greater than -5°C, and SLW was observed at temperatures near -35°C. Samples of ice at these high temperatures were often observed as precipitating ice particles below the cloud base, which may have originated at colder temperatures. Further, there appears to be a sharp decrease in the frequency of the liquid phase once temperatures drop below -20°, suggesting the possibility of ice nucleating particles being activated at these temperatures; conversely, there is a sharp increase in the frequency of the ice phase at these low temperatures. Below a temperature of -20°C, liquid phase samples are present, but relatively sparse. Approximately 500 CDP and RICE samples meet the conditions for SLW occurrence at temperatures less than -30°C, with the lowest temperatures dropping a few tenths of a degree below -35°C. Visual inspection of the images confirmed that these samples were indeed liquid, with these liquid clouds typically being sampled during the high altitude transit legs of the GV.

3.2 Mixed phase characterization

Figure 5 shows the probability distribution function of liquid water fraction within clouds identified as mixed phase for different temperature ranges, where the liquid fraction is the liquid content (*LWC*) divided by the total condensed water content (*TWC*). *LWC* and ice water content (*IWC*) are determined using LWC_{KING} and M_{2DS}, respectively. Sensitivity tests relating LWC_{KING} to M_{CDP} were found to be highly correlated for N_{CDP} >5 cm^{-3} (Figure C in supplementary material). Previous studies have shown a clear U-shaped distribution of liquid water fraction for in-cloud samples within the temperature range focused on in this study (e.g., Korolev et al., 2003; D'Alessandro et al., 2019). However, results here are only shown for mixed phase samples, which show a reasonable number of samples from $0.1<LWC/TWC<0.9$, producing relatively uniform distributions. This is consistent with the nature of mixed phase conditions observed over this region, whereby few and large ice aggregates are surrounded by swaths of SLW, which are evidently not depleted significantly by the occasional ice particle. Results show a maximum frequency at $LWC/TWC>0.9$ for the highest temperatures (-20° to 0°C) and a maximum frequency at $LWC/TWC<0.1$ for the lowest temperatures (-40° to -20°C). Interestingly, the *LWC/TWC* at -10° to 0°C is the most uniformly distributed compared to other temperature regimes, whereby the frequency at *LWC/TWC*>0.9 is lower for this regime (~0.18) compared with that from -20° to -10°C and -30° to -20°C (~0.35 and ~0.22, respectively).

Figure 6 shows multiple microphysical properties sorted by *LWC/TWC* for only those samples identified as mixed phase, whereby moving right to left along the respective abscissas corresponds to more glaciated conditions. The parameters in red correspond with CDP measurements and those in blue correspond with 2DS measurements, which generally correspond to liquid and ice phase observations, respectively. Further, mixed phase samples are restricted to those having CDP meet the definition of liquid as shown in Figure 2, which amounts to ~97% of all mixed phase samples. Figure 6A is a histogram of the *LWC/TWC* samples binned at intervals of 0.1. There is a slight peak at *LWC/TWC*<0.1 and the largest peak is at *LWC/TWC*>0.9, however, the distribution is relatively uniform.

Focusing on liquid microphysical properties, σ_{D_CDP} and *Mean* D_{CDP} increase with *LWC/TWC* until *LWC/TWC* reaches about 0.4, and then subsequently decrease (Figure 6B,C). Noting that N_{CDP} also increases with *LWC/TWC* (Figure 6D), this is consistent with smaller droplets preferentially evaporating during the WBF process, as LWC is reduced by transfer to the ice phase. This may be expected as a volume of smaller droplets has a greater total surface area relative to a volume of larger droplets having an equivalent liquid mass content. For ice phase properties, N_{2DS} slightly increases with decreasing *LWC/TWC* for *LWC/TWC* > 0.4, whereas *mean* D_{2DS} is relatively constant and begins to increase with decreasing *LWC/TWC* when *LWC/TWC*<0.4. Further, N_{2DS} decreases with decreasing LWC/TWC when LWC/TWC<0.4. Examination of 2DS particle size distributions and particle imagery show drizzle drops are often collocated at LWC/TWC>0.4, and the number of drizzle drops decreases as LWC/TWC decreases below 0.4. Because of this, caution must be taken when interpreting the 2DS results, as there may still be an overlap of ice and liquid particles.

3.3 Cloud phase spatial heterogeneity

An additional goal of this study is to describe the phase spatial heterogeneity within low-level SO cloud regimes. A novel quantitative approach to describe spatial heterogeneity is developed here. Figure 7A provides a visualization of three terms that are introduced to aid in the phase heterogeneity analysis. A sample has a time resolution of one second (~150 m). A segment is defined as a set of samples whose neighboring samples all have the same phase. A transect is defined as the total length of the cloud sampled (i.e., a set of consecutive in-cloud samples or segments with no clear air between). Utilizing these terms allows the spatial heterogeneity to be quantified by directly relating the number of samples to segments within a transect. Namely, a cloud with a greater number of segments will be more spatially heterogeneous than one with fewer segments, given similar transect lengths. Further, a completely heterogeneous cloud would have the same number of samples as segments, as the phase would change along the flight path at every second. In contrast, heterogeneity is minimized by having the minimum number of segments possible (i.e., one segment for a cloud with one phase, two segments for a cloud with two phases and three segments for a cloud with three phases). The visualization in Figure 7A is an example of a cloud transect having the minimal amount of heterogeneity, since only three segments are observed in the transect containing three phases. Increasing the number of segments would increase its spatial heterogeneity. The heterogeneity would be maximized if every sample was a different phase from its neighboring sample(s).

Figure 7B shows the length of cloud transects (derived from the true aircraft speed) related to the total length of each phase contained within the cloud transects. The results are restricted to -20°–0°C in order to focus on boundary layer clouds; and in any event, ice phase samples dominate lower temperatures. The number (percentage) of one phase transects between -20° and 0°C having at least five samples was 268 (39%), 1 (~0%), and 54 (~8%) for liquid, mixed, and ice phase conditions, respectively. For transects containing at least two phases, 369 (53%) were observed between the same temperatures. At temperatures between -40° and -20°C, 73% were one phase transects containing ice and 23% contained at least two phases.

Figure 7B does not include one phase transects, as the markers would lie directly on the one-to-one line (black line). The colored lines show average phase lengths as a function of the cloud transect length. For all transect lengths, the total length of liquid phase samples is greater than the lengths of mixed phase samples and nearly equal to or greater than the lengths of ice phase samples, as the red line is closest to the one-to-one line. This is consistent with the relative frequency distributions in Figure 4. The lengths of the ice phase samples are relatively close to those of the liquid phase samples for transect lengths less than ~4 km and closer to those of the mixed phase samples at transect lengths greater than ~4km. Overall, results reveal that the liquid phase is more frequent (i.e., has greater total lengths) than the ice phase for transects greater than 4km but is equally frequent for transects less than 4km. In addition, the mixed phase is less frequent than the ice phase for transects less than 4 km and less frequent than the liquid phase regardless of transect length, but is approximately as frequent as the ice phase for transects greater than ~5km.

Figure 7C,D shows the number of segments within a cloud transect as a function of the number of samples within the transect as black dots, whereas the number of samples and segments for each phase contained within the cloud transects are given by the colored markers. Cloud transects with greater spatial heterogeneity are generally farther up the y-axis (i.e., clouds with a relatively large number of segments will approach the one-to-one line). Overall, the datapoints are relatively scattered for the cloud and phase samples, and the best fit linear regressions (black and colored lines for the cloud and phase markers, respectively) lie between the minimum (dotted and dashed lines) and maximum (dotted dashed line) heterogeneous values. This allows for an absolute measure of the relative heterogeneity between different phases. Figure 7C shows results at temperatures between -10° and 0°C, which reveal the most spatially heterogeneous phase is the mixed phase, as the green lines have the greatest number of segments. In contrast, the least heterogeneous phase is the liquid phase, as the red lines have the least number of segments. Figure 7D shows results at temperatures between -20° and -10°C, revealing the most spatially heterogeneous phase is the mixed phase, whereas the least heterogeneous phase is the ice phase. When combining the two temperature regimes, the most heterogeneous phase is the mixed phase and the least heterogeneous is the liquid phase (Figure D in supplementary material). Further, the best fit line for cloud transects is slightly lower at -10° to 0°C compared with -20° to -10°C, as seen by the relatively similar slopes beyond ~30 samples and the solid black lines intercepting the right ordinate at ~40 segments for the warmer regime and greater than 100 segments for colder temperatures. This suggests spatial heterogeneity increases with decreasing temperature from 0° to -20°C.

To determine a quantitative measure of heterogeneity, a parameter is developed to define the spatial heterogeneity, which is called the spatial heterogeneity score (*SHS*). The equation is simply a normalization equation described as

$$\mathrm{SHS_n} = \frac{\mathrm{samples_n} - \mathrm{segments_n}}{\mathrm{samples_n} - 1} \qquad (1)$$

where n is substituted for *cld* when *SHS* is calculated for the entire transect (SHS_{cld}), and for *liq*, *mix* or *ice* when calculated for the respective phases contained within a given transect (SHS_{liq}, SHS_{mix}, SHS_{ice}). A more homogeneous cloud has SHS_{cld} approach one and a more heterogeneous cloud will have SHS_{cld} approach zero. Figure 8 shows histograms of SHS_{cld} and $SHS_{liq,mix,ice}$. The frequency of SHS_{cld} cases exceeding 0.5 far exceeds the frequency of cases less than 0.5, suggesting clouds over the SO are generally spatially homogeneous. Similarly, the frequencies of SHS_{liq} and SHS_{ice} exceeding 0.5 are much greater than those less than 0.5. In fact, nearly 50% of

SHS_{liq} and SHS_{ice} are greater than 0.9. In contrast, SHS_{mix} is nearly a uniform distribution. This is consistent with Figure 7C,D, highlighting the greater degree of spatial heterogeneity of mixed phase samples. Note the frequency distribution of SHS_{cld} has a peak frequency between 0.8 and 0.9, which may seem to conflict with SHS_{liq} and SHS_{ice} having peak frequencies greater than 0.9 and SHS_{mix} having comparable peak frequencies between 0.8 and 1.0. However, values of SHS_{cld} are inherently more heterogeneous since they always contain at least two segments for cloud transects containing at least two phases. Following the normalization equation, a cloud transect with two segments would require a minimum of 12 samples to exceed 0.9 and 22 samples for a cloud transect with three segments to likewise exceed 0.9.

The linkage between meteorological and microphysical properties to the degree of spatial heterogeneity is also investigated. An example of the analysis is shown in Figure 9 where the frequency distribution of SHS_{cld} depends on whether the sampled clouds were coupled or decoupled from the layer immediately above the ocean surface; previous studies (e.g., Wang et al., 2016; McFarquhar et al., 2021) have suggested the degree of coupling might affect cloud composition. Generally, potential temperature and moisture profiles are examined to determine coupling based on the relation between the lifting condensation level and the cloud base height. However, Wang et al. (2016) examined decoupling in subtropical environments by looking for discontinuities in vertical profiles of potential temperature, moisture content, and aerosol number concentrations. They developed a metric whereby environments are considered decoupled if the differences in the top and bottom of the subcloud layer (i.e., the cloud base and surface, respectively) potential temperature and water vapor mixing ratio exceed 1.0K and 0.6 g kg^{-1}, respectively. Otherwise, an environment is considered coupled. This metric is applied here using the nearest dropsonde profile to each cloud transect. Figure 9 shows that coupled and decoupled environments have similar distributions of SHS_{cld}, suggesting there is no relation between cloud phase heterogeneity and surface coupling.

A Whitney-Mann U-test and two-sample Kolmogorov-Smirnov test are performed on the two distributions to further evaluate their similarity. The Whitney-Mann U-test determines whether the median of one distribution is significantly greater or less than the other, whereas the two-sample Kolmogorov-Smirnov test determines the significance of the maximum absolute difference between the two cumulative frequency distributions, both of which use lookup tables. These tests are chosen since they do not require prior knowledge of the distributions' shapes. Results suggest there is no statistically significant difference between the two distributions. Both tests do not reject the null hypothesis, namely, that the distributions are similar, at a significance level of 10%.

Heterogeneity analyses are applied to other meteorological and microphysical parameters are shown in Figure 10, which provides probability density functions of 1 Hz observations of temperature, w, $Mean\ D_{2DS}$ and M_{2DS} for varying SHS. Results are shown for liquid phase (A–D), mixed phase (E–H), ice phase (I–L), and all phases combined (cloud; M–P). The liquid, mixed, ice and cloud results use SHS_{liq}, SHS_{mix}, SHS_{ice} and SHS_{cld}, respectively. In order to provide an analysis of cloud transects having comparable spatial scales, as well as allowing for the analysis of localized regions of heterogeneity within relatively long transects, transects containing more than 20 samples are split into intervals of 20 samples, which are defined as sub-transects. Additionally, a minimum of 5 samples is required for a transect to be included in the analysis (e.g., a cloud transect having 68 samples is broken up into three sub-transects, each having 20 samples and one sub-transect having 8 samples). Results were not significantly different when splitting transects into intervals of 10, 30, 40 and 50 samples (Figure E1,2,3,4 in supplementary material).

Distributions of temperature for each phase are visually relatively similar among the different heterogeneity ranges, namely, the frequencies at different ranges of *SHS* generally decrease with decreasing temperature. However, there are differences worth noting. Larger frequencies of greater SHS_{liq} and SHS_{mix} occur at temperatures greater than -5°C, suggesting more spatial heterogeneity for these phases is observed at relatively lower temperatures (Figure 10A,E) which is consistent with Figure 7C,D. In addition, more homogeneous distributions of ice are observed at temperatures less than -20°C. This is seen with probabilities of ice greater for $SHS_{ice}>0.8$ and completely homogeneous sub-transects exceeding those of lower *SHS* at temperatures less than -20°C (Figure 10I). Finally, sub-transects are generally found to increase in heterogeneity (decreasing SHS_{cld}) with decreasing temperature from -20°–0°C (Figure 10M). Other notable trends are observed for additional parameters. For example, distributions of *w* are slightly broader for spatially heterogeneous sub-transects compared with more homogeneous sub-transects (Figure 10B,F,J,N), which exhibit slightly higher peaks. Statistical tests confirmed that this difference is significant (using two-sample Kolmogorov-Smirnov tests at a significance level of 1%). This trend is most notable when examining the heterogeneity over entire sub-transects (Figure 10N), as seen by peak frequencies of ~0.29, ~0.23 and ~0.18 at w~0 m s^{-1} for completely homogeneous, $0.8<SHS_{cld}<1.0$ and $SHS_{cld}<0.8$, respectively. The broader distributions of *w* suggest stronger turbulence may be related to the increase in heterogeneity within cloud transects.

In contrast, only ice particles appear to correlate with spatial heterogeneity, as highlighted by results of *mean* D_{2DS} and M_{2DS}. M_{2DS} decreases with decreasing SHS_{mix} and SHS_{ice} (Figure

10G,K), whereas distributions are similar for varying SHS_{liq} (Figure 10C). Likewise, *mean* D_{2DS} decreases with decreasing SHS_{ice} (Figure 10 L). However, distributions of *mean* D_{2DS} are nearly identical for the liquid and mixed phase, although this is due presumably to the large number of 2DS samples containing both liquid droplets and ice particles, of which liquid droplets dominate the number concentrations and number-weighted mean. In addition, N_{CDP}, σ_{D_CDP}, and M_{CDP} were similarly analyzed (as well as N_{2DS}, horizontal windspeed, and wind direction relative to flight direction; Figure F and Figure G in supplementary material, respectively) and were found to be similarly distributed regardless of *SHS*.

The distributions of the microphysical properties do not show any relation with SHS_{cld}, i.e., when observations from all phases are combined (Figure 10O,P). This is most likely due to the similarly distributed liquid phase data at varying ranges of SHS_{liq} (Figure 10C,D) smoothing out the combined liquid, mixed and ice phase distributions used with SHS_{cld}. Thus, differences are only observed in the microphysical properties of ice particles when related to the spatial heterogeneity of their respective phases and not that of the overall cloud sub-transects.

4. **Discussion**

In-cloud samples are determined to be either liquid, ice or mixed phase using a combination of cloud probes (CDP, RICE and 2DS). Potential caveats of the proposed phase classification method include the inability to discern whether a sample of particles having D<50 μm includes both ice and liquid particles. Further, a degree of subjectivity is inherent when visually classifying particles having D>50 μm. Aspherical particles can appear spherical in 2DS imagery, and spherical particles may even be frozen drops. However, it was shown in Section 2.2 that CDP and RICE can be used as a proxy to infer whether the phase of the larger particles was correctly classified. Additionally, ice is often expected to be associated with larger particle sizes, as theory dictates that under most conditions near water saturation, ice particles will quickly grow larger than droplets, such as in the types of cloud regimes sampled during SOCRATES. It is also important to note that the aircraft would have experienced significant icing and aborted in-cloud measurements if flown through regions of large SLW containing large droplet sizes at temperatures below which kinetic heating fails to offset below-freezing ambient temperatures, although SLW contents are often low in clouds sampled during SOCRATES. However, the most noticeable uncertainty of the phase ID is discerning supercooled drizzle (associated with minimal aircraft icing) and precipitating ice. While caution was taken to visually examine samples of precipitation, this may introduce slight biases in the frequency of liquid and ice phase samples primarily from -10° to 0°C (samples below cloud base) in Figure 4. Overall, the observational strategy discussed in section 2 provides a relatively uniform in-cloud sampling distribution to minimize any sampling bias associated with the structure of boundary layer clouds.

In situ measurements cannot be used to examine the evolution of mixed phase conditions in a Lagrangian framework, due to the aircraft's inability to sample an air parcel throughout its trajectory, which was not a major objective of the SOCRATES flights used in this study. However, theoretical and modeling studies show the evolution of mixed phase volumes almost always transitions from mostly liquid to all ice (e.g., when the WBF process and/or riming dominates). Therefore, by examining mixed phase samples as a function of *LWC/TWC,* different microphysical properties can be ascertained, where values near 1 depict conditions before the start of the glaciation process and values approaching 0 correspond to complete glaciation.

Figure 5 reveals U-shaped distributions in the frequency distribution of *LWC/TWC* for mixed phase samples, showing relatively uniform distributions from -20° to 0°C and distributions resembling inverse exponential functions from -40° to -20°C. Samples from all temperatures are combined in Figure 6A, revealing an exponential shape consistent with the study of McFarquhar et al. (2007a). They also sampled stratocumulus boundary layer clouds, but over the Arctic, finding a relatively uniform distribution of *LWC/TWC* near cloud base with an increasing frequency of LWC/TWC>0.9 towards cloud top in single layer stratocumulus mixed phase clouds. The uniform distribution of LWC/TWC near cloud base is consistent with results in Figure 5, which show the most uniform distributions of LWC/TWC at -10° to 0°C, which generally includes most samples near the base of the lowest cloud layers.

Liquid number concentrations decrease as *LWC/TWC* decreases, whereas the number weighted mean *D* and σ_D of liquid drops increase as *LWC/TWC* decreases. This may be due to smaller droplets preferentially evaporating at the expense of the larger droplets. Secondary ice production mechanisms (e.g., Field et al., 2017) may also play a role in these trends. Flight scientists on the G-V during SOCRATES often found drizzle collocated with ice particles, potentially suggesting that precipitation can be induced while the WBF process is acting (discussed in flight reports such as RF05, RF12, RF15). Korolev (2007) performed a box model study highlighting that the WBF process only occurs given prerequisite background requirements and discusses the range of vertical velocities whereby WBF can occur. The study found that both ice crystals and liquid drops could grow given sufficient updraft speeds. Another potential mechanism may be the removal of smaller liquid droplets via accretion. This is consistent with the increase in N_{2DS} as *LWC/TWC* decreases from 1.0 to 0.4, which could be related to secondary ice production such as rime splintering activating via accretion (i.e., the Hallett-Mossop process).

Results examining the spatial heterogeneity of liquid, mixed and ice phase occurrence within clouds suggest the mixed phase appears to be the most spatially heterogeneous. Further, SHS_{cld} are often between 0.6 and 1.0, suggesting relatively homogeneous regions often occur within transects along with "pockets" of increased heterogeneity, such as that observed in Figure 3 around 02:28:50 UTC. In fact, results in Figure 10 are split up into sub-transects in order to focus on localized regions of heterogeneity within larger transects. Such localized regions of heterogeneity, associated with "pockets" of ice and mixed phase within large swaths of supercooled liquid, could be nucleating via heterogenous nucleation. Recent work has highlighted the relatively sparse but present ice nucleating particles observed over this region (e.g., Finlon et al., 2020; McCluskey et al., 2018).

The existence of small-scale generating cells at cloud top may also be impacting the heterogeneity as Wang et al. (2020) showed that the horizontal scales of generating cells from which the precipitation emanates range from approximately 200 to 800 m, smaller than those observed over the mid-latitudes (Rosenow et al., 2014) or the Arctic (McFarquhar et al., 2011). Further, the lengths of cloud segments may be directly related to generating cells, as segment lengths are often within the range of generating cells as described in Wang et al. (2020) for lower *SHS*. However, they found number concentrations of particles having D>200 μm (of which ice particles dominate) were greater within generating cells compared with outside of them. Work presented here shows the mass and number-weighted mean D of ice particles generally decreases as cloud segments decrease in horizontal length (i.e., increase in spatial heterogeneity). Additionally, a similar analysis was performed on N_{2DS} having D>200 μm as in Figure 10 (Figure H in supplementary material) and values slightly decreased with increasing spatial heterogeneity. However, Wang et al. (2020) only selected 16 selected flight legs for analysis, when the GV aircraft was sampling near cloud top. Future work will focus on relating spatial heterogeneity to physical features within the environment.

A physical reason describing the decrease in M_{2DS} and $Mean_{2DS}$ with increasing heterogeneity may be related to cloud lifetimes. If *SHS* is considered as a proxy for the evolution/lifecycle of a cloud region, whereby "pockets" of supercooled liquid nucleate and freezing events spread spatially, then lower SHS_{liq} and higher SHS_{ice} would be expected with an "aged" cloud region. This would be consistent with the increase of ice mass and mean *D* (and relatively constant liquid mass and number concentrations) observed with increasing homogeneity.

In situ data are the measurements best suited for determining the heterogeneity of phases in SO clouds, and this has important implications for modeling studies. Zhang et al. (2019) showed that parameterizing mixed phase clouds as pockets within supercooled cloud fields for arctic clouds improved model agreement with observed liquid water contents from in situ observations taken during the Mixed Phase Arctic Cloud Experiment (Verlinde et al., 2007). Tan & Storelvmo (2016) performed a quasi-Monte Carlo sampling of varying parameters in the Community Atmospheric Model version 5.1 (CAM5) and found the vapor depletion rates associated with the WBF process contributed to the greatest amount of variance of the mass partitioning of mixed phase clouds. They further tested CAM5 for the spatial heterogeneity of phase by parameterizing mixed phase clouds as having "pockets" of liquid and ice versus the assumption of ice and liquid as homogeneously mixed, and found the simulations improved cloud macro-scale features when compared to satellite observations. They noted that the assumption of mixed phase clouds as homogenously mixed ice and liquid particles in the model results in irregularly large rates of vapor depletion, rapidly evaporating liquid at the expense of ice growth. The results presented here confirm that mixed phase regions are often on the scale of 100 m to 10 km, and adjusting models to parameterize the spatial distribution of phase as such will increase cloud fraction and lifetimes, which in turn may improve representations of radiative profiles over the SO.

5. Conclusions

The purpose of this study is to present the characteristics of cloud phase over the Southern Ocean using airborne in situ observations acquired during SOCRATES, which primarily sampled low-level clouds over the Southern Ocean. The relative phase frequencies controlled by temperature reveal an exceptionally large frequency of supercooled liquid between -20° and 0°C. Ice was observed at temperatures near freezing and supercooled liquid at temperatures near -35°C. A sharp decrease in supercooled liquid was observed once temperatures dropped below -20°C, suggesting that the activation of ice nucleating particles might be the primary influence on the presence of different cloud phases. This is consistent with similar findings of a sharp increase in ice phase occurrence frequencies observed over Cape Grim, Tasmania (Alexander & Protat, 2018).

The spatial heterogeneity of cloud phase is examined by relating the number and lengths of different cloud phases contained within each cloud. A metric is also introduced which diagnoses a degree of spatial heterogeneity to each cloud sampled. Results show that most clouds are relatively spatially homogeneous as highlighted in Figures 7C,D and 8. The spatial heterogeneity of specific phases are also examined, and results show that the mixed phase is the most spatially heterogeneous from -20° to 0°C, whereas the liquid phase is the least spatially heterogeneous from -10° to 0°C and the ice phase from -20° to -10°C. Correctly characterizing the spatial heterogeneity of low-level clouds over the SO is crucial, as assumptions on phase mixing can have major impacts on cloud cover, lifetime, and microphysical properties.

Finally, local microphysical and meteorological properties are related to the spatial heterogeneity of both the individual phases and of the cloud transects. Transects generally increase in heterogeneity with decreasing temperature from -20° to 0°C, and the distribution of w slightly broadens with decreasing SHS_{cld}. In addition, the mass and mean diameter of ice particles are found to decrease with increasing heterogeneity. Future work will further examine the trends of microphysical properties in relation to spatial heterogeneity.

Acknowledgement: This work was supported by the National Science Foundation (NSF) through grants AGS-1628674 and AGS-1762096. This material is based upon work supported by the National Center for Atmospheric Research, which is a major facility sponsored by the National Science Foundation under Cooperative Agreement No. 1852977. The data were collected using NSF's Lower Atmosphere Observing Facilities, which are managed and operated by NCAR's Earth Observing Laboratory. The NSF SOCRATES campaign dataset is publicly available and can be accessed at http://www.eol.ucar.edu/field_projects/socrates. We thank the pilots, mechanics, technicians, scientists, software engineers, and project managers of the NCAR EOL Research Aviation Facility for their support in the field and in post-processing data. We would like to thank the Australian Bureau of Meteorology Tasmanian regional Office for the excellent forecast support and weather briefings provided during the field campaign with special thanks to Scott Carpentier, Michelle Hollister, Matthew Thomas and Robert Schaap.

References

Alexander, S. P., & Protat, A. (2018). Cloud Properties Observed From the Surface and by Satellite at the Northern Edge of the Southern Ocean. *Journal of Geophysical Research:*

Atmospheres, *123*(1), 443–456. https://doi.org/10.1002/2017JD026552

Baumgardner, D., Abel, S. J., Axisa, D., Cotton, R., Crosier, J., Field, P., et al. (2017). Cloud Ice Properties: In Situ Measurement Challenges. *Meteorological Monographs*, *58*(1), 9.1-9.23. https://doi.org/10.1175/amsmonographs-d-16-0011.1

Baumgardner, D., & Korolev, A. (1997). Airspeed corrections for optical array probe sample volumes. *Journal of Atmospheric and Oceanic Technology*, *14*(5), 1224–1229. https://doi.org/10.1175/1520-0426(1997)014<1224:ACFOAP>2.0.CO;2

Bergeron, T. (1928). Über die dreidimensional verknüpfende Wetteranalyse. *Geophys. Norv.*, *5*(6), 1–111.

Bergeron, T. (1935). On the physics of clouds and precipitation. *Proces Verbaux de l'Association de Météorologie, International Union of Geodesy and Geophysics*, 156–178.

Bishop, C. (2006). Pattern Recognition and Machine Learning.

Biter, C. J., Dye, J. E., Huffman, D., & King, W. D. (1987). The Drop-Size Response of the CSIRO Liquid Water Probe. *Journal of Atmospheric and Oceanic Technology*, *4*(3), 359–367. https://doi.org/10.1175/1520-0426(1987)004<0359:TDSROT>2.0.CO;2

Bodas-Salcedo, A., Hill, P. G., Furtado, K., Williams, K. D., Field, P. R., Manners, J. C., et al. (2016). Large Contribution of Supercooled Liquid Clouds to the Solar Radiation Budget of the Southern Ocean. *Journal of Climate*, *29*(11), 4213–4228. https://doi.org/10.1175/JCLI-D-15-0564.1

Ceppi, P., Zelinka, M. D., & Hartmann, D. L. (2014). The response of the Southern Hemispheric eddy-driven jet to future changes in shortwave radiation in CMIP5. *Geophysical Research*

Letters, *41*(9), 3244–3250. https://doi.org/10.1002/2014GL060043

Cesana, G., & Chepfer, H. (2013). Evaluation of the cloud thermodynamic phase in a climate model using CALIPSO-GOCCP. *Journal of Geophysical Research: Atmospheres*, *118*(14), 7922–7937. https://doi.org/10.1002/jgrd.50376

Chylek, P., Robinson, S., Dubey, M. K., King, M. D., Fu, Q., & Clodius, W. B. (2006). Comparison of near-infrared and thermal infrared cloud phase detections. *Journal of Geophysical Research*, *111*(D20), D20203. https://doi.org/10.1029/2006JD007140

Cober, S. G., Isaac, G. A., Korolev, A. V., & Strapp, J. W. (2001). Assessing Cloud-Phase Conditions. *Journal of Applied Meteorology*, *40*(11), 1967–1983. https://doi.org/10.1175/1520-0450(2001)040<1967:ACPC>2.0.CO;2

Cooper, W. A., Friesen, R. B., Hayman, M., Jensen, J. B., Lenschow, D. H., Romashkin, P. A., et al. (2016). *Characterization of Uncertainty in Measurements of Wind From the NSF/NCAR Gulfstream V Research Aircraft*. Retrieved from https://opensky.ucar.edu/islandora/object/technotes%3A540/datastream/PDF/view

D'Alessandro, J. J., Diao, M., Wu, C., Liu, X., Jensen, J. B., & Stephens, B. B. (2019). Cloud phase and relative humidity distributions over the Southern Ocean in austral summer based on in situ observations and CAM5 simulations. *Journal of Climate*, *32*(10), 2781–2805. https://doi.org/10.1175/JCLI-D-18-0232.1

EOL. (2018). SOCRATES (2018) Project Manager Report. Retrieved from https://www.eol.ucar.edu/system/files/SOCRATES PM Report.pdf

Field, P. R., Wood, R., Brown, P. R. A., Kaye, P. H., Hirst, E., Greenaway, R., & Smith, J. A.

(2003). Ice particle interarrival times measured with a fast FSSP. *Journal of Atmospheric and Oceanic Technology*, *20*(2), 249–261. https://doi.org/10.1175/1520-0426(2003)020<0249:IPITMW>2.0.CO;2

Field, P. R., Lawson, R. P., Brown, P. R. A., Lloyd, G., Westbrook, C., Moisseev, D., et al. (2017). Secondary Ice Production - current state of the science and recommendations for the future. *Meteorological Monographs*, 7.1-7.20. https://doi.org/10.1175/amsmonographs-d-16-0014.1

Field, P. R., Hogan, R. J., Brown, P. R. A., Illingworth, A. J., Choularton, T. W., Kaye, P. H., et al. (2004). Simultaneous radar and aircraft observations of mixed-phase cloud at the 100 m scale. *Quarterly Journal of the Royal Meteorological Society*, *130*(600), 1877–1904. https://doi.org/10.1256/qj.03.102

Field, P. R., Heymsfield, A. J., & Bansemer, A. (2006). Shattering and particle interarrival times measured by optical array probes in ice clouds. *Journal of Atmospheric and Oceanic Technology*, *23*(10), 1357–1371. https://doi.org/10.1175/JTECH1922.1

Findeisen, W. (1938). Kolloid-meteorologische Vorgänge bei Neiderschlags-bildung. *Meteorologische Zeitschrift*, *55*, 121–133.

Findeisen, W. (1940). On the origin of thunderstorm electricity. *Meteorologische Zeitschrift*, *57*, 201–215.

Finlon, J. A., McFarquhar, G. M., Nesbitt, S. W., Rauber, R. M., Morrison, H., Wu, W., & Zhang, P. (2019). A novel approach for characterizing the variability in mass–dimension relationships: results from MC3E. *Atmospheric Chemistry and Physics*, *19*(6), 3621–3643. https://doi.org/10.5194/acp-19-3621-2019

Finlon, J. A., Rauber, R. M., Wu, W., Zaremba, T. J., McFarquhar, G. M., Nesbitt, S. W., et al. (2020). Structure of an Atmospheric River Over Australia and the Southern Ocean: II. Microphysical Evolution. *Journal of Geophysical Research: Atmospheres*, *125*(18). https://doi.org/10.1029/2020JD032514

Frey, W. R., & Kay, J. E. (2017). The influence of extratropical cloud phase and amount feedbacks on climate sensitivity. *Climate Dynamics*, 1–20. https://doi.org/10.1007/s00382-017-3796-5

Gettelman, A., & Sherwood, S. C. (2016). Processes Responsible for Cloud Feedback. *Current Climate Change Reports*, *2*(4), 179–189. https://doi.org/10.1007/s40641-016-0052-8

Heymsfield, A. J., & Miloshevich, L. M. (1989). Evaluation of Liquid Water Measuring Instruments in Cold Clouds Sampled during FIRE. *Journal of Atmospheric and Oceanic Technology*, *6*(3), 378–388. https://doi.org/10.1175/1520-0426(1989)006<0378:EOLWMI>2.0.CO;2

Heymsfield, A. J., Field, P. R., Bailey, M., Rogers, D., Stith, J., Twohy, C., et al. (2011). Ice in clouds experiment-layer clouds. Part I: Ice growth rates derived from lenticular wave cloud penetrations. *Journal of the Atmospheric Sciences*, *68*(11), 2628–2654. https://doi.org/10.1175/JAS-D-11-025.1

Holroyd, E. W. (1987). Some Techniques and Uses of 2D-C Habit Classification Software for Snow Particles. *Journal of Atmospheric and Oceanic Technology*, *4*(3), 498–511. https://doi.org/10.1175/1520-0426(1987)004<0498:stauoc>2.0.co;2

Huang, Y., Siems, S. T., Manton, M. J., Thompson, G., Huang, Y., Siems, S. T., et al. (2014). An Evaluation of WRF Simulations of Clouds over the Southern Ocean with A-Train

Observations. *Monthly Weather Review*, *142*(2), 647–667. https://doi.org/10.1175/MWR-D-13-00128.1

Huang, Y., Franklin, C. N., Siems, S. T., Manton, M. J., Chubb, T., Lock, A., et al. (2015). Evaluation of boundary-layer cloud forecasts over the Southern Ocean in a limited-area numerical weather prediction system using in situ , space-borne and ground-based observations. *Quarterly Journal of the Royal Meteorological Society*, *141*(691), 2259–2276. https://doi.org/10.1002/qj.2519

Jackson, R. C., McFarquhar, G. M., Korolev, A. V., Earle, M. E., Liu, P. S. K., Lawson, R. P., et al. (2012). The dependence of ice microphysics on aerosol concentration in arctic mixed-phase stratus clouds during ISDAC and M-PACE. *Journal of Geophysical Research Atmospheres*, *117*(15). https://doi.org/10.1029/2012JD017668

Jackson, R. C., Mcfarquhar, G. M., Stith, J., Beals, M., Shaw, R. A., Jensen, J., et al. (2014). An assessment of the impact of antishattering tips and artifact removal techniques on cloud ice size distributions measured by the 2D cloud probe. *Journal of Atmospheric and Oceanic Technology*, *31*(12), 2567–2590. https://doi.org/10.1175/JTECH-D-13-00239.1

Jolliffe, I. T., & Stephenson, D. B. (2011). Forecast Verification: A Practitioner's Guide in Atmospheric Science, 2nd Edition. Retrieved from https://www.wiley.com/en-us/Forecast+Verification%3A+A+Practitioner%27s+Guide+in+Atmospheric+Science%2C+2nd+Edition-p-9780470660713

Kay, J. E., Hillman, B. R., Klein, S. A., Zhang, Y., Medeiros, B., Pincus, R., et al. (2012). Exposing Global Cloud Biases in the Community Atmosphere Model (CAM) Using Satellite Observations and Their Corresponding Instrument Simulators. *Journal of Climate*, *25*(15), 5190–5207. https://doi.org/10.1175/JCLI-D-11-00469.1

Kay, J. E., Wall, C., Yettella, V., Medeiros, B., Hannay, C., Caldwell, P., & Bitz, C. (2016). Global Climate Impacts of Fixing the Southern Ocean Shortwave Radiation Bias in the Community Earth System Model (CESM). *Journal of Climate*, *29*(12), 4617–4636. https://doi.org/10.1175/JCLI-D-15-0358.1

King, W. D., Parkin, D. A., & Handsworth, R. J. (1978). A Hot-Wire Liquid Water Device Having Fully Calculable Response Characteristics. *Journal of Applied Meteorology*, *17*(12), 1809–1813. https://doi.org/10.1175/1520-0450(1978)017<1809:AHWLWD>2.0.CO;2

Korolev, A. V., McFarquhar, G., Field, P. R., Franklin, C., Lawson, P., Wang, Z., et al. (2017). Mixed-Phase Clouds: Progress and Challenges. *Meteorological Monographs*, *58*, 5.1-5.50. https://doi.org/10.1175/AMSMONOGRAPHS-D-17-0001.1

Korolev, A. V. (2007). Limitations of the Wegener–Bergeron–Findeisen Mechanism in the Evolution of Mixed-Phase Clouds. *Journal of the Atmospheric Sciences*, *64*(9), 3372–3375. https://doi.org/10.1175/JAS4035.1

Korolev, A. V., & Field, P. R. (2008). The Effect of Dynamics on Mixed-Phase Clouds: Theoretical Considerations. *Journal of the Atmospheric Sciences*, *65*(1), 66–86. https://doi.org/10.1175/2007JAS2355.1

Korolev, A. V., & Isaac, G. A. (2006). Relative Humidity in Liquid, Mixed-Phase, and Ice Clouds. *Journal of the Atmospheric Sciences*, *63*(11), 2865–2880. https://doi.org/10.1175/JAS3784.1

Korolev, A. V., Isaac, G. A., Cober, S. G., Strapp, J. W., & Hallett, J. (2003). Microphysical characterization of mixed-phase clouds. *Quarterly Journal of the Royal Meteorological Society*, *129*(587), 39–65. https://doi.org/10.1256/qj.01.204

Kreidenweis, S. M., Petters, M., & Lohmann, U. (2018). 100 years of progress in cloud physics, aerosols, and aerosol chemistry research. *Meteorological Monographs*, *59*, 11.1-11.72. https://doi.org/10.1175/AMSMONOGRAPHS-D-18-0024.1

Lance, S., Brock, C. A., Rogers, D., & Gordon, J. A. (2010). Water droplet calibration of the Cloud Droplet Probe (CDP) and in-flight performance in liquid, ice and mixed-phase clouds during ARCPAC. *Atmospheric Measurement Techniques*, *3*(6), 1683–1706. https://doi.org/10.5194/amt-3-1683-2010

Lawson, R. P., & Gettelman, A. (2014). Impact of Antarctic mixed-phase clouds on climate. *Proceedings of the National Academy of Sciences of the United States of America*, *111*(51), 18156–61. https://doi.org/10.1073/pnas.1418197111

Matus, A. V., & L'Ecuyer, T. S. (2017). The role of cloud phase in Earth's radiation budget. *Journal of Geophysical Research: Atmospheres*, *122*(5), 2559–2578. https://doi.org/10.1002/2016JD025951

Mazin, I. P., Korolev, A. V., Heymsfield, A., Isaac, G. A., & Cober, S. G. (2001). Thermodynamics of Icing Cylinder for Measurements of Liquid Water Content in Supercooled Clouds. *Journal of Atmospheric and Oceanic Technology*, *18*(4), 543–558. https://doi.org/10.1175/1520-0426(2001)018<0543:TOICFM>2.0.CO;2

McCluskey, C. S., Hill, T. C. J., Humphries, R. S., Rauker, A. M., Moreau, S., Strutton, P. G., et al. (2018). Observations of Ice Nucleating Particles Over Southern Ocean Waters. *Geophysical Research Letters*, *45*(21), 11,989-11,997.

https://doi.org/10.1029/2018GL079981

McCoy, D. T., Hartmann, D. L., & Grosvenor, D. P. (2014). Observed Southern Ocean Cloud Properties and Shortwave Reflection. Part II: Phase Changes and Low Cloud Feedback*. *Journal of Climate*, *27*(23), 8858–8868. https://doi.org/10.1175/JCLI-D-14-00288.1

McFarquhar, G. M., Um, J., Freer, M., Baumgardner, D., Kok, G. L., & Mace, G. (2007b). Importance of small ice crystals to cirrus properties: Observations from the Tropical Warm Pool International Cloud Experiment (TWP-ICE). *Geophysical Research Letters*, *34*(13). https://doi.org/10.1029/2007GL029865

McFarquhar, G. M., Finlon, J. A., Stechman, D. M., Wu, W., & Jackson, Robert M. Freer, M. (2018). University of Illinois/Oklahoma Optical Array Probe (OAP) Processing Software. Version 3.1.4. Zenodo. https://doi.org/doi:http://doi.org/10.5281/

McFarquhar, G. M., Zhang, G., Poellot, M. R., Kok, G. L., McCoy, R., Tooman, T., et al. (2007a). Ice properties of single-layer stratocumulus during the Mixed-Phase Arctic Cloud Experiment: 1. Observations. *Journal of Geophysical Research*, *112*(D24), D24201. https://doi.org/10.1029/2007JD008633

McFarquhar, G. M., Ghan, S., Verlinde, J., Korolev, A., Strapp, J. W., Schmid, B., et al. (2011). Indirect and semi-direct aerosol campaign: The impact of arctic aerosols on clouds. *Bulletin of the American Meteorological Society*, *92*(2), 183–201. https://doi.org/10.1175/2010BAMS2935.1

McFarquhar, G. M., & Cober, S. G. (2004). Single-scattering properties of mixed-phase Arctic clouds at solar wavelengths: Impacts on radiative transfer. *Journal of Climate*, *17*(19), 3799–3813. https://doi.org/10.1175/1520-0442(2004)017<3799:SPOMAC>2.0.CO;2

McFarquhar, G. M., Baumgardner, D., Bansemer, A., Abel, S. J., Crosier, J., French, J., et al. (2017). Processing of Ice Cloud In Situ Data Collected by Bulk Water, Scattering, and Imaging Probes: Fundamentals, Uncertainties, and Efforts toward Consistency. *Meteorological Monographs*, *58*, 11.1-11.33. https://doi.org/10.1175/amsmonographs-d-16-0007.1

McFarquhar, G. M., Bretherton, C., Marchand, R., Protat, A., DeMott, P. J., Alexander, S. P., et al. (2021). Observations of clouds, aerosols, precipitation, and surface radiation over the Southern Ocean: An overview of CAPRICORN, MARCUS, MICRE and SOCRATES. *Bulletin of the American Meteorological Society*, *102*(4), E894–E928. https://doi.org/10.1175/bams-d-20-0132.1

Mitchell, J. F. B., Senior, C. A., & Ingram, W. J. (1989). C02 and climate: a missing feedback? *Nature*, *341*(6238), 132–134. https://doi.org/10.1038/341132a0

Morrison, H., de Boer, G., Feingold, G., Harrington, J., Shupe, M. D., & Sulia, K. (2012). Resilience of persistent Arctic mixed-phase clouds. *Nature Geoscience*, *5*(1), 11–17. https://doi.org/10.1038/ngeo1332

Murphy, D. M., & Koop, T. (2005). Review of the vapour pressures of ice and supercooled water for atmospheric applications. *Quarterly Journal of the Royal Meteorological Society*, *131*(608), 1539–1565. https://doi.org/10.1256/qj.04.94

Naud, C. M., Booth, J. F., & Del Genio, A. D. (2014). Evaluation of ERA-Interim and MERRA cloudiness in the southern ocean. *Journal of Climate*, *27*(5), 2109–2124. https://doi.org/10.1175/JCLI-D-13-00432.1

Praz, C., Ding, S., McFarquhar, G. M., & Berne, A. (2018). A Versatile Method for Ice Particle

Habit Classification Using Airborne Imaging Probe Data. *Journal of Geophysical Research: Atmospheres*, *123*(23), 13,472-13,495. https://doi.org/10.1029/2018JD029163

Rosenow, A. A., Plummer, D. M., Rauber, R. M., McFarquhar, G. M., Jewett, B. F., & Leon, D. (2014). Vertical velocity and physical structure of generating cells and convection in the comma head region of continental winter cyclones. *Journal of the Atmospheric Sciences*, *71*(5), 1538–1558. https://doi.org/10.1175/JAS-D-13-0249.1

Schwarzenboeck, A., Mioche, G., Armetta, A., Herber, A., & Gayet, J.-F. (2009). Response of the Nevzorov hot wire probe in clouds dominated by droplet conditions in the drizzle size range. *Atmospheric Measurement Techniques*, *2*(2), 779–788. https://doi.org/10.5194/amt-2-779-2009

Shupe, M. D., & Intrieri, J. M. (2004). Cloud Radiative Forcing of the Arctic Surface: The Influence of Cloud Properties, Surface Albedo, and Solar Zenith Angle. *Journal of Climate*, *17*(3), 616–628. https://doi.org/10.1175/1520-0442(2004)017<0616:CRFOTA>2.0.CO;2

Storelvmo, T., Kristjánsson, J. E., & Lohmann, U. (2008). Aerosol Influence on Mixed-Phase Clouds in CAM-Oslo. *Journal of the Atmospheric Sciences*, *65*(10), 3214–3230. https://doi.org/10.1175/2008JAS2430.1

Stubenrauch, C. J., Rossow, W. B., Scott, N. A., & Chédin, A. (1999). Clouds as seen by satellite sounders (3I) and imagers (ISCCP). Part III: Spatial heterogeneity and radiative effects. *Journal of Climate*, *12*(12), 3419–3442. https://doi.org/10.1175/1520-0442(1999)012<3419:CASBSS>2.0.CO;2

Sun, Z., & Shine, K. P. (1994). Studies of the radiative properties of ice and mixed-phase clouds. *Quarterly Journal of the Royal Meteorological Society*, *120*(515), 111–137.

https://doi.org/10.1002/qj.49712051508

Tan, I., Storelvmo, T., & Zelinka, M. D. (2016). Observational constraints on mixed-phase clouds imply higher climate sensitivity. *Science*, *352*(6282), 224–227. https://doi.org/10.1126/science.aad5300

Tan, I., & Storelvmo, T. (2016). Sensitivity Study on the Influence of Cloud Microphysical Parameters on Mixed-Phase Cloud Thermodynamic Phase Partitioning in CAM5. *Journal of the Atmospheric Sciences*, *73*(2), 709–728. https://doi.org/10.1175/JAS-D-15-0152.1

Trenberth, K. E., & Fasullo, J. T. (2010). Simulation of Present-Day and Twenty-First-Century Energy Budgets of the Southern Oceans. *Journal of Climate*, *23*(2), 440–454. https://doi.org/10.1175/2009JCLI3152.1

Tsushima, Y., Emori, S., Ogura, T., Kimoto, M., Webb, M. J., Williams, K. D., et al. (2006). Importance of the mixed-phase cloud distribution in the control climate for assessing the response of clouds to carbon dioxide increase: a multi-model study. *Climate Dynamics*, *27*(2–3), 113–126. https://doi.org/10.1007/s00382-006-0127-7

Verlinde, J., Harrington, J. Y., McFarquhar, G. M., Yannuzzi, V. T., Avramov, A., Greenberg, S., et al. (2007). The mixed-phase arctic cloud experiment. *Bulletin of the American Meteorological Society*, *88*(2), 205–221. https://doi.org/10.1175/BAMS-88-2-205

Wang, Y., McFarquhar, G. M., Rauber, R. M., Zhao, C., Wu, W., Finlon, J. A., et al. (2020). Microphysical Properties of Generating Cells Over the Southern Ocean: Results From SOCRATES. *Journal of Geophysical Research: Atmospheres*, *125*(13). https://doi.org/10.1029/2019JD032237

Wang, Y., Zhang, D., Liu, X., & Wang, Z. (2018). Distinct Contributions of Ice Nucleation, Large-Scale Environment, and Shallow Cumulus Detrainment to Cloud Phase Partitioning With NCAR CAM5. *Journal of Geophysical Research: Atmospheres*, *123*(2), 1132–1154. https://doi.org/10.1002/2017JD027213

Wang, Z., Mora Ramirez, M., Dadashazar, H., MacDonald, A. B., Crosbie, E., Bates, K. H., et al. (2016). Contrasting cloud composition between coupled and decoupled marine boundary layer clouds. *Journal of Geophysical Research: Atmospheres*, *121*(19), 11,679-11,691. https://doi.org/10.1002/2016JD025695

Wegener, A. (1911). *Thermodynamik der Atmosphäre*. J. A. Barth.

Wu, W., & McFarquhar, G. M. (2019). NSF/NCAR GV Hiaper fast 2DS particle size distribution (psd) product data. Version 1.1. UCAR/NCAR-Earth Observing Laboratorytle. https://doi.org/https://doi.org/10.26023/8hmg-wqp3-xa0x

Zaremba, T. J., Rauber, R. M., McFarquhar, G. M., Hayman, M., Finlon, J. A., & Stechman, D. M. (2020). Phase Characterization of Cold Sector Southern Ocean Cloud Tops: Results from SOCRATES. *Journal of Geophysical Research: Atmospheres*. https://doi.org/10.1029/2020JD033673

Zhang, M., Liu, X., Diao, M., D'Alessandro, J. J., Wang, Y., Wu, C., et al. (2019). Impacts of Representing Heterogeneous Distribution of Cloud Liquid and Ice on Phase Partitioning of Arctic Mixed-Phase Clouds with NCAR CAM5. *Journal of Geophysical Research: Atmospheres*, *124*(23), 13071–13090. https://doi.org/10.1029/2019JD030502

Zondlo, M. A., Paige, M. E., Massick, S. M., & Silver, J. A. (2010). Vertical cavity laser hygrometer for the National Science Foundation Gulfstream-V aircraft. *Journal of*

Geophysical Research, *115*(D20), D20309. https://doi.org/10.1029/2010JD014445

	Instrument	**Measurement**	**Uncertainties**	**Manufacturer**
Bulk cloud properties	Cloud droplet probe (CDP)	size distribution (2-50μm)	Uncertain size distribution of non-spherical particles	DMT
	Two-dimensional Stereo probe (2DS)	size distribution (10-1280μm)	Highly uncertain depth of field at D<50μm	SPEC, Inc.
	Rosemount Icing Detector (RICE)	presence of SLW	Theoretical threshold liquid water content limit of ~0.025 g m^{-3} or less	Rosemount
	KING probe	liquid water content	Underestimates liquid water content in presence of drizzle	DMT
Additional instrumentation	Rosemount temperature probe	temperature	Accuracy of 0.3 K Precision 0.01 K	Rosemount
	Radome gust probe, inertial system, and GPS	vertical air speed	Net uncertainty of 0.12 m s^{-1} (likely higher uncertainty for SOCRATES)	–
	25-Hz Vertical Cavity Surface Emitting Laser (VCSEL) hygrometer	water vapor	Accuracy of ~6% Precision of 1%	Southwest Sciences Inc.

Table 1: A list of all instrumentation and relevant information used in this study. Sources related to uncertainties are contained within Section 2.

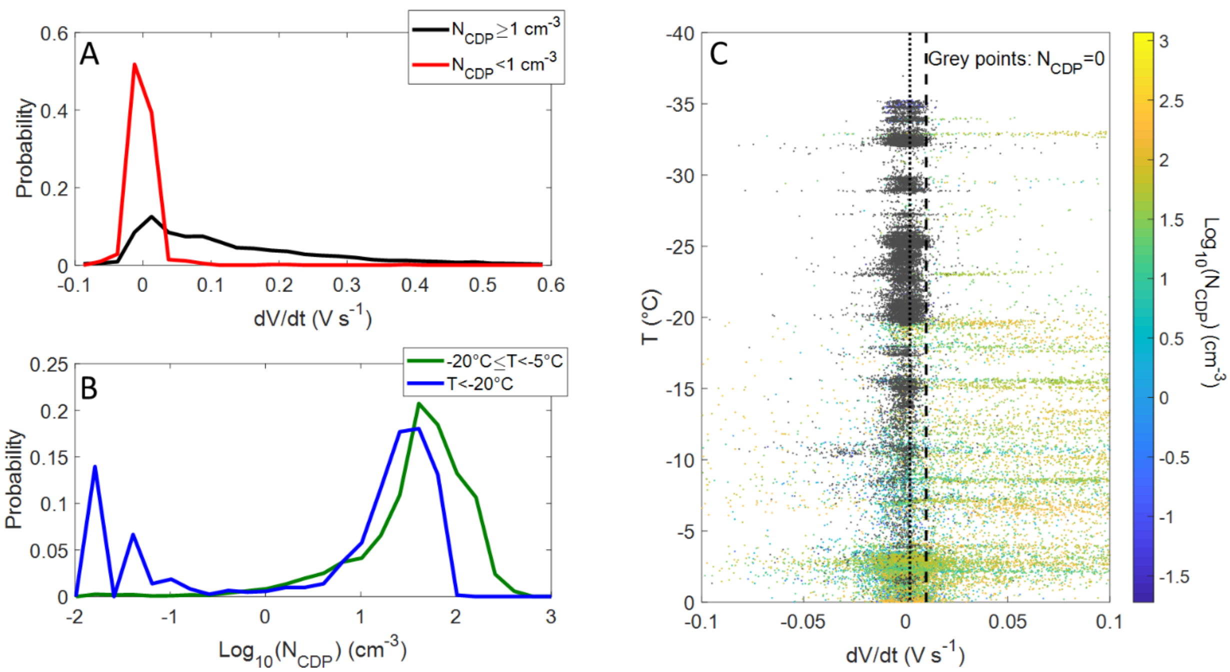

Figure 1: Probability distribution function of dV/dt of RICE for $N_{CDP}\geq1$ cm^{-3} and $N_{CDP}<1$ cm^{-3} (A), as well as for N_{CDP} at temperatures from -20° to -5°C and less than -20°C (B). Vertical profile of dV/dt colored by N_{CDP} (C). Samples in 1A,B are all considered in-cloud for CDP (i.e., $M_{CDP}\geq10^{-3}$ g m^{-3}) and in 1C for CDP or 2DS ($M_{CDP}\geq10^{-3}$ g m^{-3} or $N_{2DS}>0$). The grey points in 1C represent in-cloud samples having $N_{CDP}=0$. The dotted and dashed lines are at 0.002 V s^{-1} and 0.01 V s^{-1}, respectively.

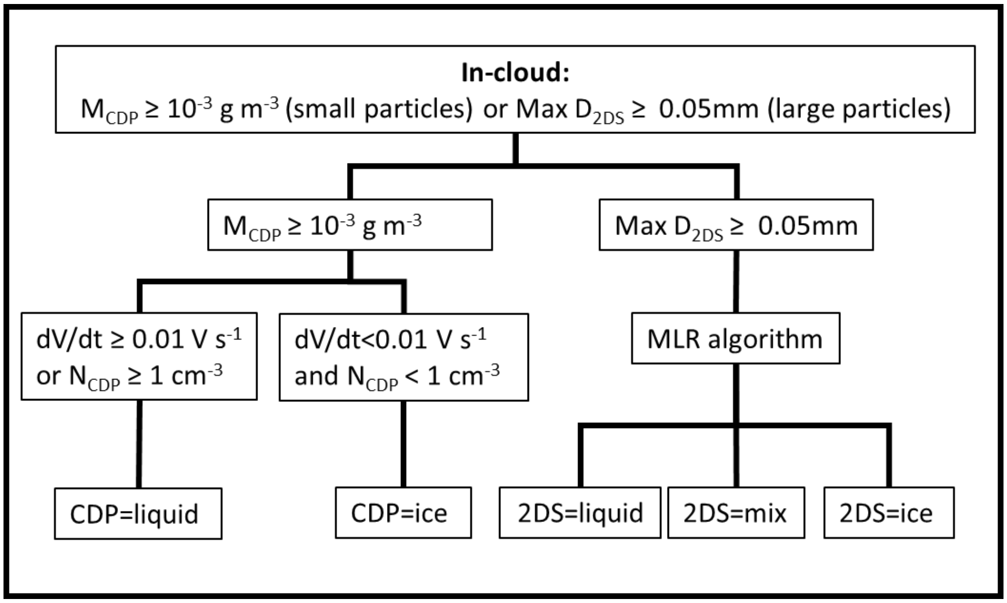

Figure 2: Flow chart highlighting how phase is determined using the CDP, RICE and 2DS probes. The phase is reported for every second, whereby the combination of CDP and 2DS phases determines the phase at every second (e.g., CDP=liquid and Max D_{2DS}<0.05 mm is classified as liquid, CDP=liquid and 2DS=ice is classified as mixed phase, etc.).

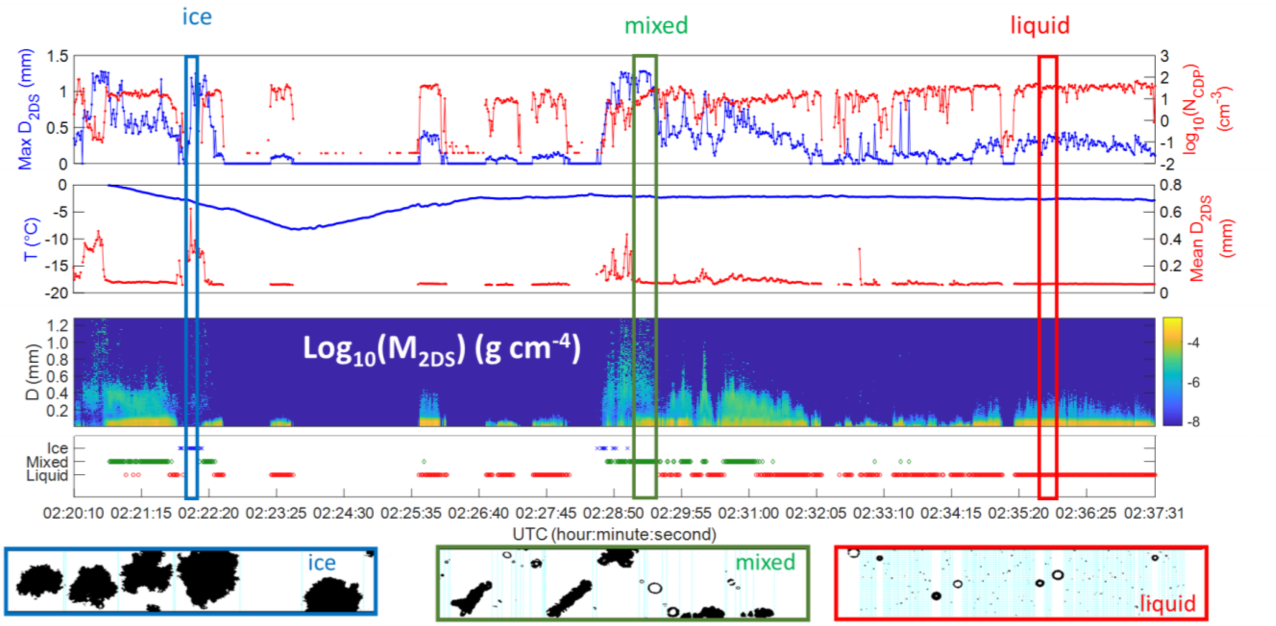

Figure 3: Time series from RF06 showing Max D_{2DS} and N_{CDP} (top row), temperature and number weighted mean D_{2DS} (2nd row), the mass size distribution normalized by bin width (3rd) and the phase derived from the phase algorithm in Figure 2 (bottom row). The red, green and blue boxes correspond with underlying 2DS optical array imagery of liquid, mixed and ice phase samples, respectively.

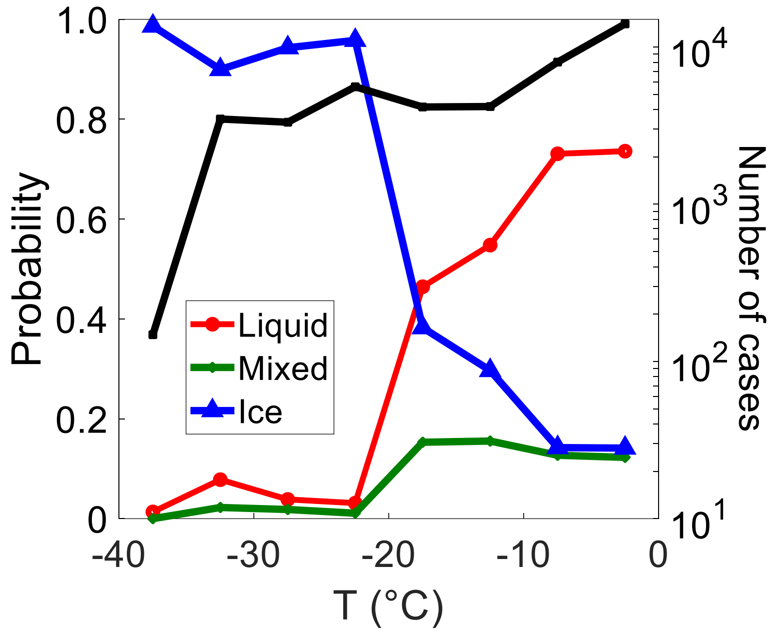

Figure 4: The relative frequency distribution of liquid, mixed and ice phase samples are shown as the colored lines, whereas the number of in-cloud samples from the SOCRATES campaign is shown by the black line. Results are binned at 5°C intervals.

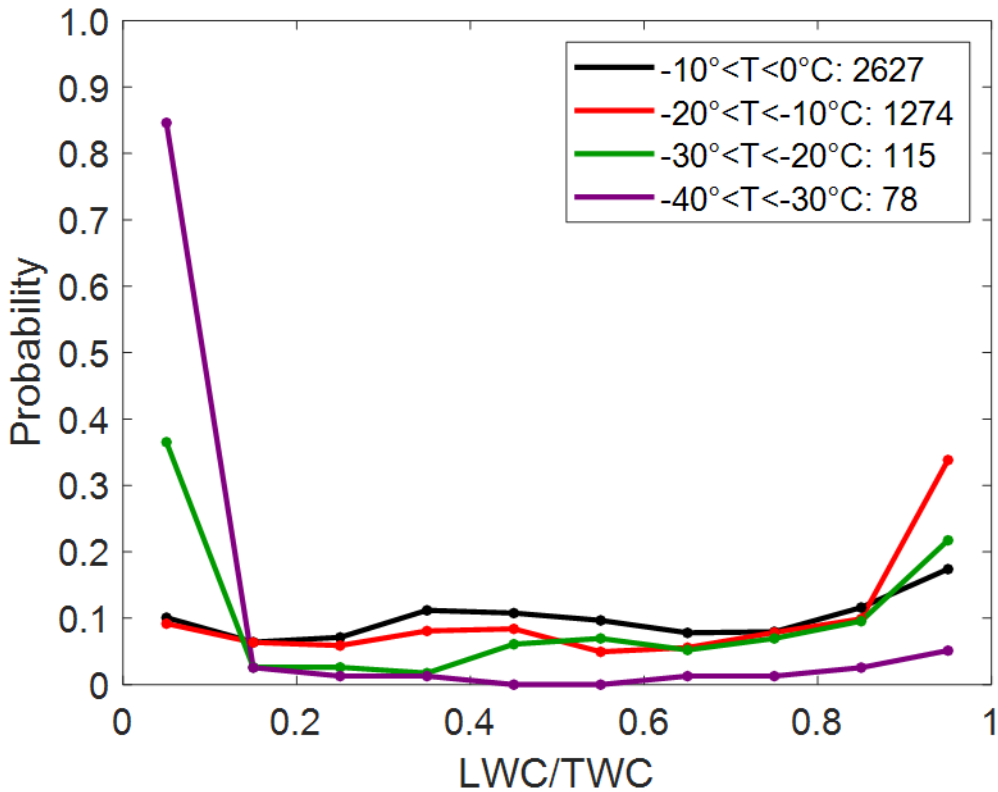

Figure 5: Probability density functions of liquid to total condensate mass ratio for SOCRATES. Results are only shown for mixed phase cases. Different colored lines correspond with different temperature regimes. The number of samples for each temperature regime is provided in the legend.

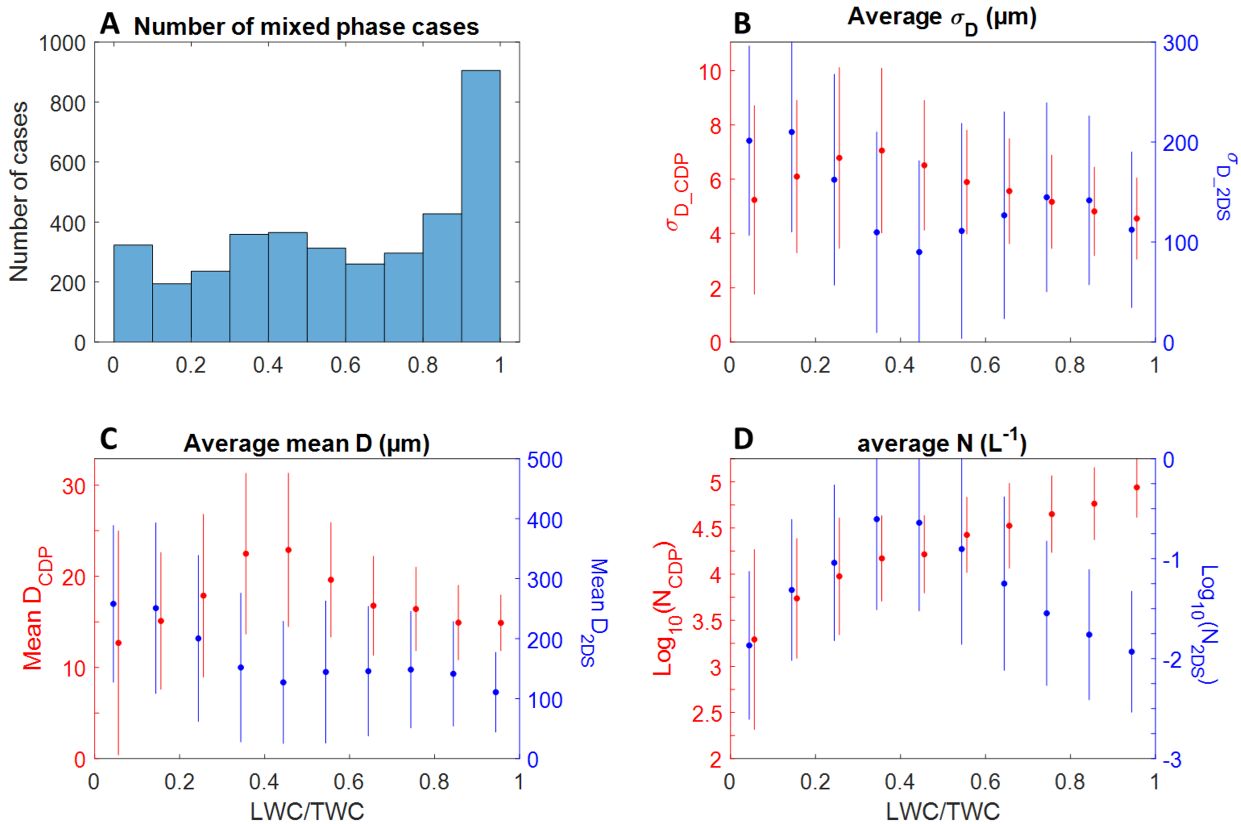

Figure 6: Number of 1 second samples for analysis (A). The mean values of σ_D (B), number weighted *mean D* (C) and *N* (D) of CDP and 2DS observations controlled by *LWC/TWC*. Colored lines represent one standard deviation. Results are shown for the CDP (2DS) in red (blue) and are primarily representative of liquid (ice) particles. Results are restricted to mixed phase samples where CDP is classified as liquid.

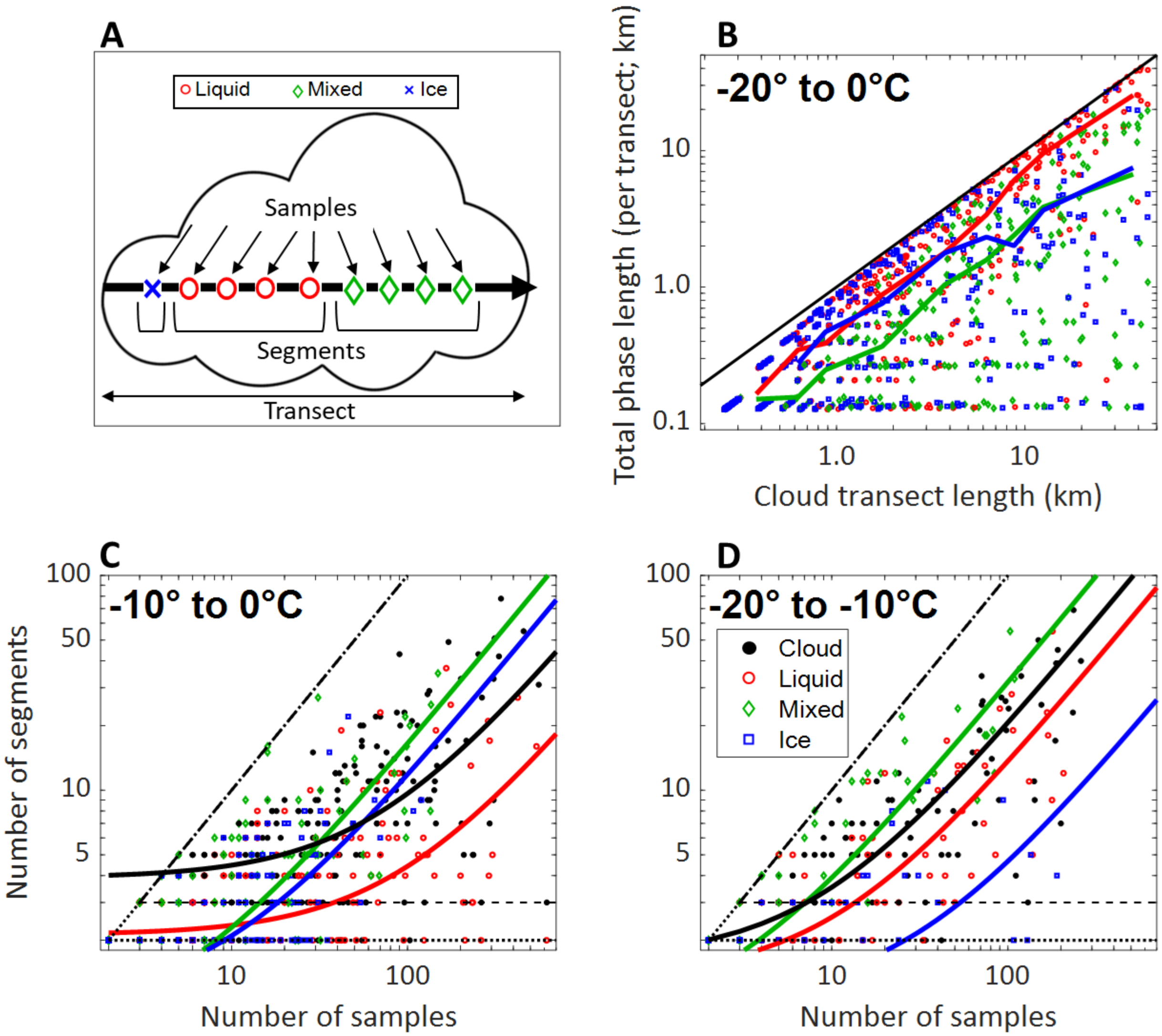

Figure 7: An idealized diagram highlighting the introduced terms “samples”, “segments” and “transects” (A), a scatterplot of the cloud transect length versus the total length of the respective phases (colored markers) contained within the transects (B) and the number of samples of a cloud transect (black dots) and phase contained within a cloud transect (colored markers) versus the respective number of segments (C,D). Results in 7B,C,D are restricted to temperature ranges shown in their respective panels, and cloud transects containing at least two phases. Colored lines in 7B show average phase lengths. The lines in 7C,D are best fit linear regressions for the

respective phases (colored lines) and entire cloud transects (black line). The black line in 7B shows the one-to-one line. The dotted (dashed) line in 7C,D represents the minimal possible heterogeneity for cloud transects containing two (three) phases. The dotted dashed line represents a completely heterogeneous cloud (i.e., the number of samples equals the number of segments). The markers in 7B,C correspond with those shown in the legend of 7D.

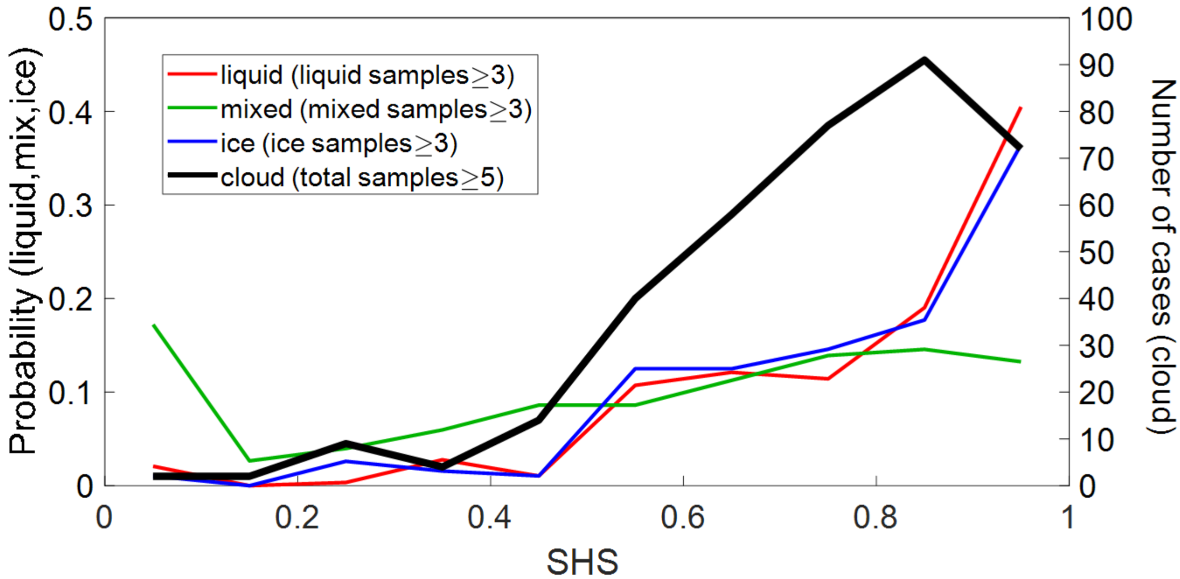

Figure 8: Histogram of SHS_{cld} (black line; right ordinate) and probability density functions of SHS_{liq}, SHS_{mix} and SHS_{ice} (colored lines; left ordinate). The results are restricted similar to Figure 7B, as well as limited for a given number of samples (shown in the legend).

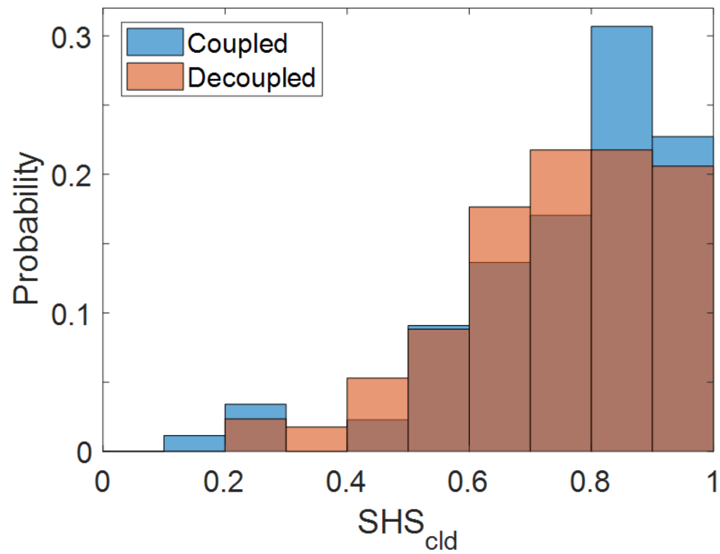

Figure 9: Probability density function of SHS_{cld} for coupled and decoupled environments. SHS_{cld} are only shown for cloud transects with ≥5 samples as in Figure 8. Coupling is determined following Wang et al. (2016) whereby the nearest dropsonde to a given cloud transect is used.

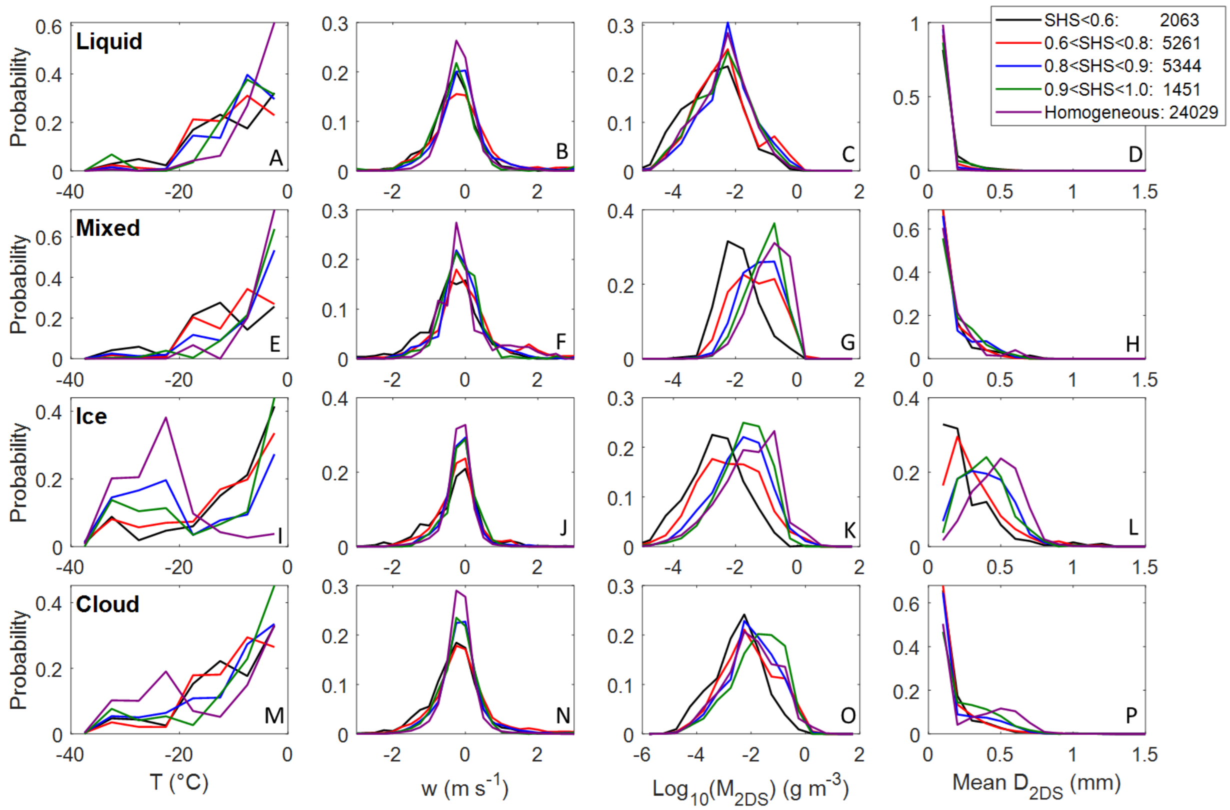

Figure 10: Probability density functions of temperature (leftmost column), *w* (left column), M_{2DS} (right column) and *Mean* D_{2DS} (rightmost column) for varying ranges of *SHS*. Results are shown for liquid (A–D), mixed (E–H), ice (I–L) and all phases combined (cloud; M–P). Analyses of liquid, mixed, ice and cloud samples are applied using SHS_{liq}, SHS_{mix}, SHS_{ice} and SHS_{cld}, respectively. Cloud transects longer than 20 samples are broken down into intervals of 20 samples. Transects shorter than 20 samples must contain at least 5 samples. The number of samples for each range of SHS_{cld} are included in the legend. Homogeneous represents transects containing only one phase.